*Solid State Phenomena*
*ISSN: 1662-9779, Vol. 388, pp 209-225*
*doi:10.4028/p-bY5Ylk*

*Submitted: 2026-01-19*
*Revised: 2026-02-14*
*Accepted: 2026-02-21*
*Online: 2026-04-15*

# Springback Prediction of 6XXX-Series Aluminum: Effect of Hardening Model, Friction and Binder Loading

Joseph Arciero[1,a*], Kenneth Cheong[1,b], Mahmoud Howeyze[1,c], Isaura Escorza[2,d], Akshay Wankhede[2,e], Kidambi Kannan[2,f], Sarin Thokala[3,g], Christian Leppin[4,h], David Anderson[3,i], Cliff Butcher[1,j]

[1]Department of Mechanical and Mechatronics Engineering, University of Waterloo, ON, Canada

[2]AutoForm Engineering, Troy, Michigan, USA

[3]Novelis, Kennesaw, Georgia, USA

[4]Novelis, Sierre, Switzerland

[a*]jarciero@uwaterloo.ca, [b]dwkcheong@uwaterloo.ca, [c]mhoweyze@uwaterloo.ca, [d]isaura.escorza@autoform.com, [e]akshay.wankhede@autoform.com, [f]kidambi.kannan@autoform.com, [g]sarin.thokala@novelis.adityabirla.com, [h]christian.leppin@novelis.adityabirla.com, [i]david.anderson@novelis.adityabirla.com, [j]cbutcher@uwaterloo.ca

[*]Corresponding author email: jarciero@uwaterloo.ca

**Keywords:** sheet metal forming, kinematic hardening, AutoForm, TriboForm.

**Abstract.** Predicting the final shape of automotive structural components after springback is a challenge to the inclusion of high strength aluminum alloys into the vehicle body-in-white. Complex deformation paths and reverse loading of sheet material during forming operations can induce significant Bauschinger effects and kinematic hardening behaviour. Capturing the through-thickness stress gradient is critical when predicting springback, which is governed by tooling dynamics, frictional forces, and material plasticity. In this study, the anisotropic behaviour of a AA6xxx-T4 aluminum alloy was characterized to calibrate a BBC2005 yield function, kinematic hardening effects were characterized through a novel uniaxial compression-tension technique, and a technology demonstrator U-shaped rail component was formed and scanned to assess the final shape after springback. Multiple model variations were analyzed in AutoForm R12, modifying simulation control parameters, binder loading condition (uniform vs. column), friction model (Coulomb vs. TriboForm), and hardening model (isotropic vs. kinematic). The use of column binder loading paired with TriboForm friction model provided the most significant improvement for thinning and springback prediction accuracy with kinematic hardening being a second order effect compared to accounting for friction and binder force.

## Introduction

To improve vehicle range while maintaining increasing crash safety standards, the automotive industry is turning towards high-strength steel and aluminum alloys to produce lightweight vehicle architectures [1,2]. AA6xxx and AA7xxx series aluminum sheet metal alloys are particularly promising with strength-to-weight ratios comparable to high strength steel with one third the density. However, accurate springback prediction remains a key challenge to overcome in the adoption of thicker, higher strength aluminum alloys into structural body-in-white components.

The forming of complex components involves non-linear deformation paths and bending-unbending as the material flows over drawbeads into the die cavity. This loading can activate significant Bauschinger effects and transient hardening [3] that requires the use of kinematic hardening models to improve springback predictions [4-6]. Solfronk *et al*. [6] used the relatively complex Yoshida-Uemori kinematic hardening model [7] to improve predicted final shape after U-bending AA6111 while Bong *et al*. [8] obtained good springback predictions using the simpler

Chaboche kinematic hardening model with a Yld2000 criterion for three-point bend testing of AA6061-T6.

Although accurate characterization of anisotropic plasticity and hardening behaviour is essential, springback prediction depends equally, if not more, on the proper representation of the tooling and frictional forces that dictate material flow and the severity of the through thickness stress and strain gradients. Frictional behaviour in forming simulations is often simplified using constant Coulomb friction with typical friction coefficients between 0.1 to 0.2 [9]. Lee [10] demonstrated that within this amount of friction variation, predicted sidewall curl of U-shaped drawn channels may vary up to 24%. Pressure- and velocity-dependent friction models are now being used in forming simulations for improved springback, thickness, and formability predictions [9,11-13]. Advanced friction models such as TriboForm®, describe the dependence of friction coefficient on contact pressure, plastic strain, and temperature for a given combination of material, surface topography, and lubricant [14]. The application of TriboForm® friction models have been shown to improve springback and formability predictive capabilities compared to Coulomb friction in the work of Bolay *et al*. [15] and Berahmani *et al.* [16].

The objective of this study is to detail the improvement of springback predictions of an industrially-representative U-shaped rail section for a AA6xxx-T4 aluminum as a function of the simulation control parameters, kinematic hardening, and friction model. Tensile, plane strain notch, shear, and biaxial tests were performed to characterize the anisotropic behaviour in proportional loading while compression-tension tests were used to characterize kinematic hardening effects. Multiple permutations of the forming model were analyzed in AutoForm R12 with an emphasis on the choice of binder loading conditions, friction, and hardening models.

## 2. Constitutive and Formability Characterization

The material of interest is a 2 mm thick 6xxx-series aluminum alloy in the T4 temper, which is similar to a AA6111-T4. Uniaxial tension, plane strain notch, and shear tests were performed in multiple orientations with the geometries depicted in Fig. 1. The tensile properties obtained in the rolling (RD), diagonal (DD), and transverse (TD) directions are summarized in Table 1. The engineering stress-strain response from a representative RD test is shown in Fig. 2.

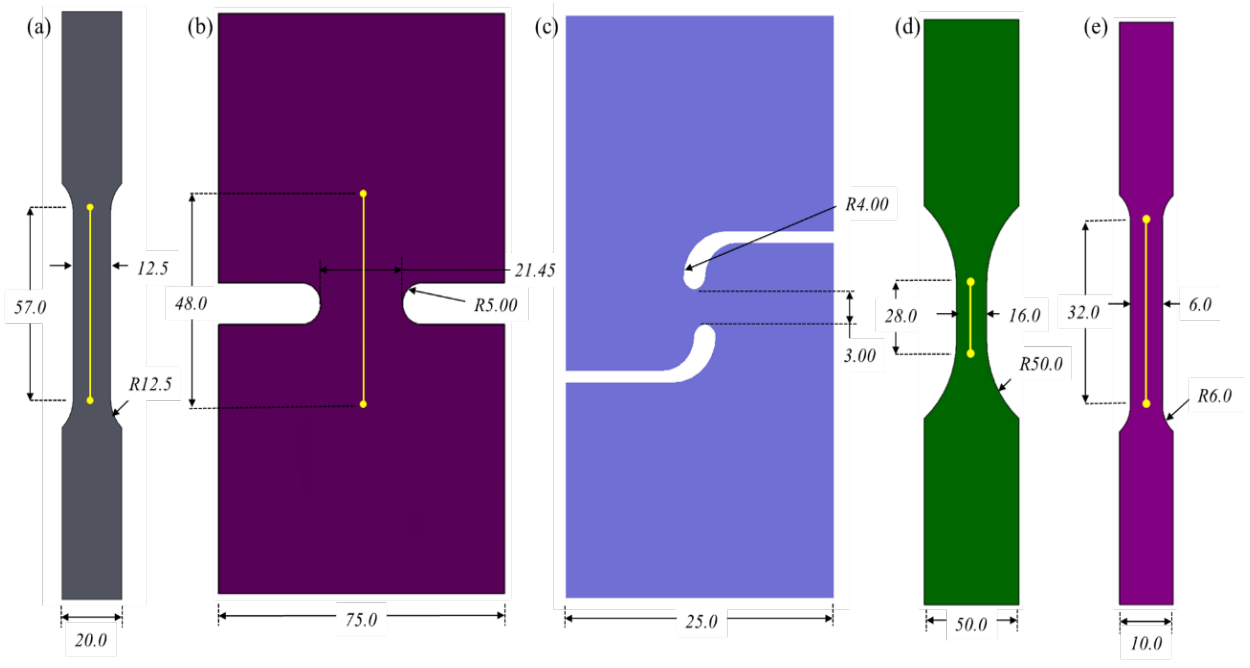


**Fig. 1.** (a) ASTM E8 tensile specimen [17], (b) plane strain notch specimen, (c) shear test geometry, (d) tension-compression test geometry, and (e) Subsized ASTM E8 specimen [17]. Yellow lines denote extensometers. Note: schematic shown is not to scale. All units in mm.

**Table 1.** Tensile properties of the AA6xxx-T4 material with standard deviation. YS yield strength, UTS ultimate tensile strength, UE uniform elongation, TE total elongation. Four test repeats performed per orientation.

| Direction | Tensile Geometry | 0.2% YS [MPa] | UTS [MPa] | UE [%] | TE [%] |
|---|---|---|---|---|---|
| RD | ASTM E8 | 154.0 ± 0.0 | 273 ± 1.0 | 21.0 ± 0.6 | 25.8 ± 1.1 |
| DD | | 150.0 ± 1.0 | 272 ± 1.0 | 24.2 ± 0.6 | 29.6 ± 0.8 |
| TD | | 149.0 ± 0.0 | 270.0 ± 0.0 | 21.9 ± 1.8 | 25.5 ± 1.4 |

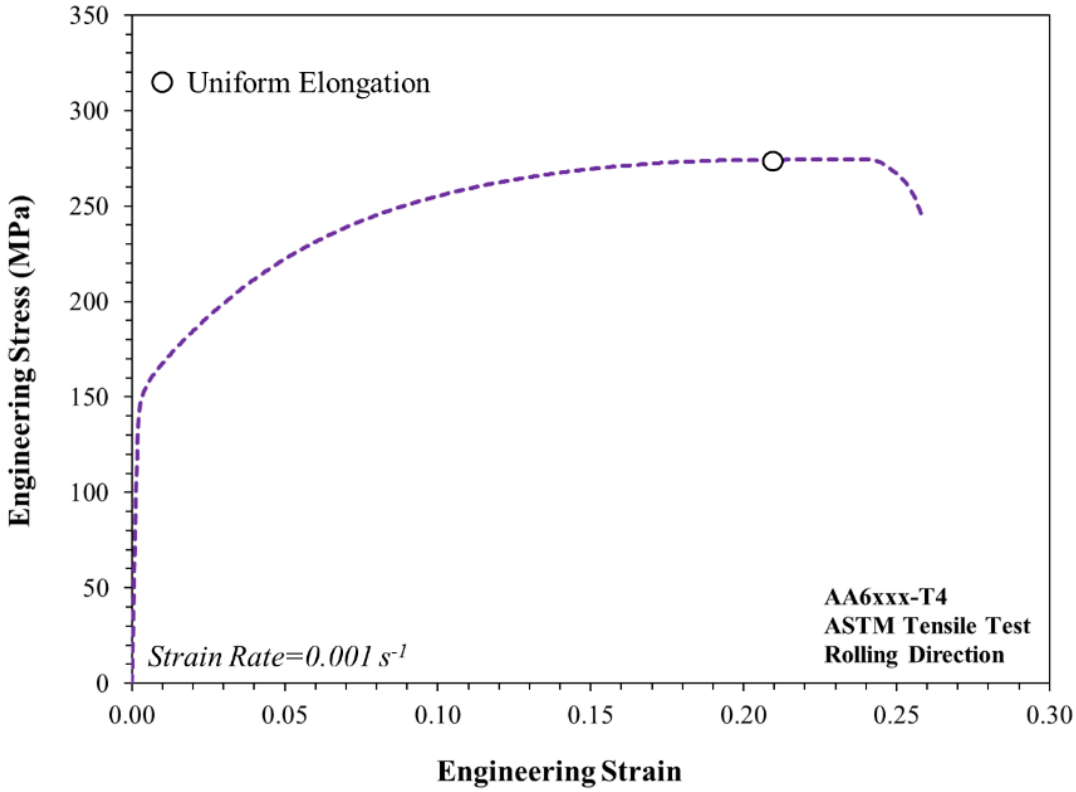


**Fig. 2.** Engineering stress-strain response of AA6xxx-T4 material along the rolling direction with uniform elongation indicated.

Interrupted disc compression tests at multiple strain levels were conducted to obtain the biaxial R-value ($R_B$). Hydraulic bulge tests were performed according to ISO 16808 [19] to obtain the biaxial stress-strain response and determine the biaxial stress ratio ($\sigma_B$). Simple shear tests were performed to determine the shear stress ($\tau$) response using the methodology of Narayanan *et al.* [20]. Plane strain notch tests were performed in RD, DD and TD using the specimen geometry depicted in Fig. 1b. The notch geometry induces a strong strain gradient from plane strain at notch center to uniaxial at the free edge. Plane strain condition was verified by extracting the local strain evolution at the notch center using a point inspector in Vic-3D® software from correlated solutions following the procedures of Narayanan *et al.* [21]. Local strain evolution at the notch center from a representative plane strain notch test in RD is shown in Fig. 3.

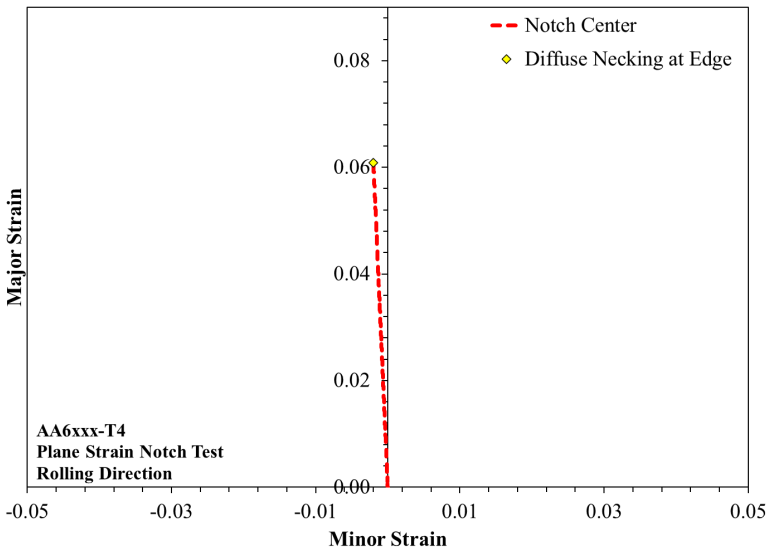


**Fig. 3.** Local strain evolution of 6xxx-T4 material at notch center of plane strain notch test in RD.

Table 2 summarizes the normalized yield stress ratios relative to RD and plastic strain anisotropy in various directions at a plastic work level of 40 MJ/m$^3$. Fig. 4a depicts calibrated Yld2000 [22] and BBC2005 [23] yield surfaces for the AA6xxx-T4. The BBC2005 yield surface was calibrated within AutoForm R12 and exhibits close agreement with Yld2000, which is included as a comparative reference due to its widespread use in literature. Constrained inverse FE analysis of plane strain notch tests in the RD, DD and TD were performed according to the methodology developed in Abedini *et al*. [18] to determine the local arc of the yield function from uniaxial to plane strain tension. The yield surface exponent identified from the notch tests was larger than the commonly assumed value of 8 for FCC materials and set to a value of 16 in Yld2000 and 12 in BBC2005, which is the maximum available value within AutoForm R12. Yield exponents larger than 8 have also been experimentally observed for a 6016-T4 by Kuwabara *et al.* [24] using stress-controlled cruciform tests with values on the order of 22.7.

**Table 2.** Normalized tensile, plane strain (PS), and shear yield stresses relative to RD tensile stress, R-values at various orientations for the AA6xxx-T4 material at a plastic work of 40 MJ/m$^3$.

| Parameter | Experimental Average & Standard Deviation |
|---|---|
| $\sigma_{RD}/\sigma_{RD}$ | 1.000 ± 0.004 |
| $\sigma_{DD}/\sigma_{RD}$ | 0.986 ± 0.007 |
| $\sigma_{TD}/\sigma_{RD}$ | 0.989 ± 0.006 |
| $(\sigma_{PS}/\sigma_{RD})$ | 1.024 ± 0.004 |
| $\sigma_B/\sigma_{RD}$ | 0.989 ± 0.009 |
| $\tau_{RD}/\sigma_{RD}$ | 0.570 ± 0.007 |
| $\tau_{DD}/\sigma_{RD}$ | 0.581 ± 0.007 |
| $\tau_{TD}/\sigma_{RD}$ | 0.565 ± 0.005 |
| $R_{RD}$ | 0.684 ± 0.024 |
| $R_{DD}$ | 0.570 ± 0.017 |
| $R_{TD}$ | 0.805 ± 0.012 |
| $R_B$ | 0.830 ± 0.020 |

The area reduction method (ARM) of Abedini *et al.* [25] was employed to allow for characterization of the hardening response beyond uniform elongation. The cross-section shape of the neck was monitored using stereo-DIC following which the average area strain and stresses were estimated. Correction factors of Choung and Cho [26] were applied to account for change in stress

state due to necking, enabling the characterization of the hardening response to 40% strain compared to the uniform elongation strain of 21% in RD. Fig. 4b is the hardening response of the AA6xxx-T4 material along RD, DD, TD directions. The reader is referred to Abedini *et al.* [25] for further details regarding the ARM.

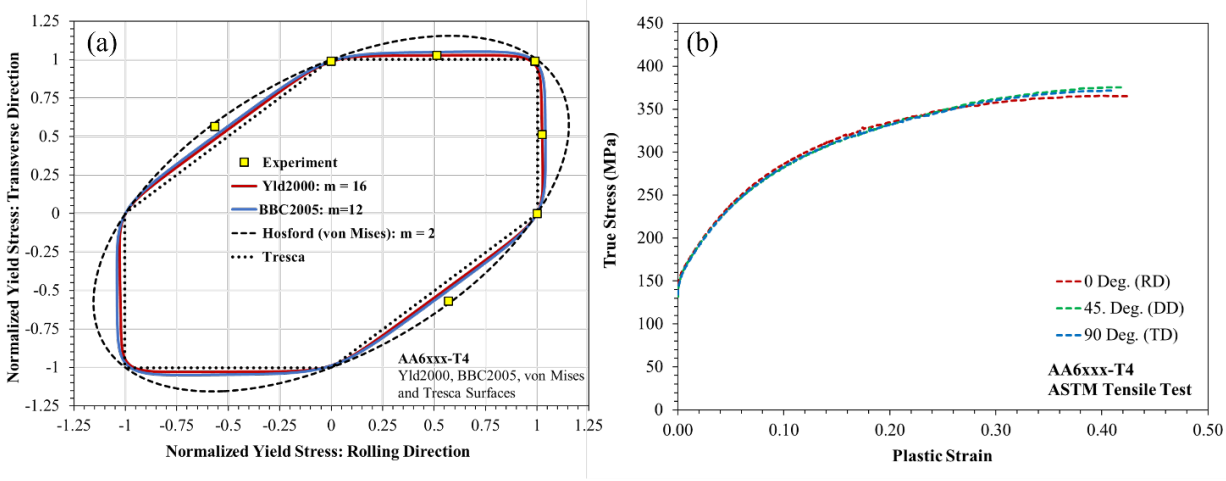


**Fig. 4.** (a) Calibrated Yld2000 and BBC2005 yield surfaces overlayed with von Mises and Tresca, and (b) the hardening response in RD, DD, and TD for the AA6xxx-T4 alloy.

Kinematic hardening effects were characterized through a novel uniaxial compression-tension testing technique using the specimen geometry depicted in Fig. 1d. This technique makes use of a tension-compression test fixture, shown in Fig. 5, designed and developed at the University of Waterloo with integrated in-plane DIC. The test setup consists of two axial load cells, the second of which added for friction measurements, as first done by Banerjee *et al.* [27]. The anti-buckling fixture applies a side load to the test specimen via a nitrogen spring, contacting the specimen through steel and Gorilla® glass inserts, depicted in Fig. 5b. The glass window allows for planar DIC strain measurements, facilitated through the front mounted camera. A representative compression-tension (CT) cycle with 5.5% pre-strain is shown in Fig 8. The CT data was corrected to account for friction and contact stress using a plastic work analysis as well as accounting for the asymmetric friction distribution that emerges when one grip is stationary. Details on the correction methodology are provided in the work of Pilozo-Hibbit [28].

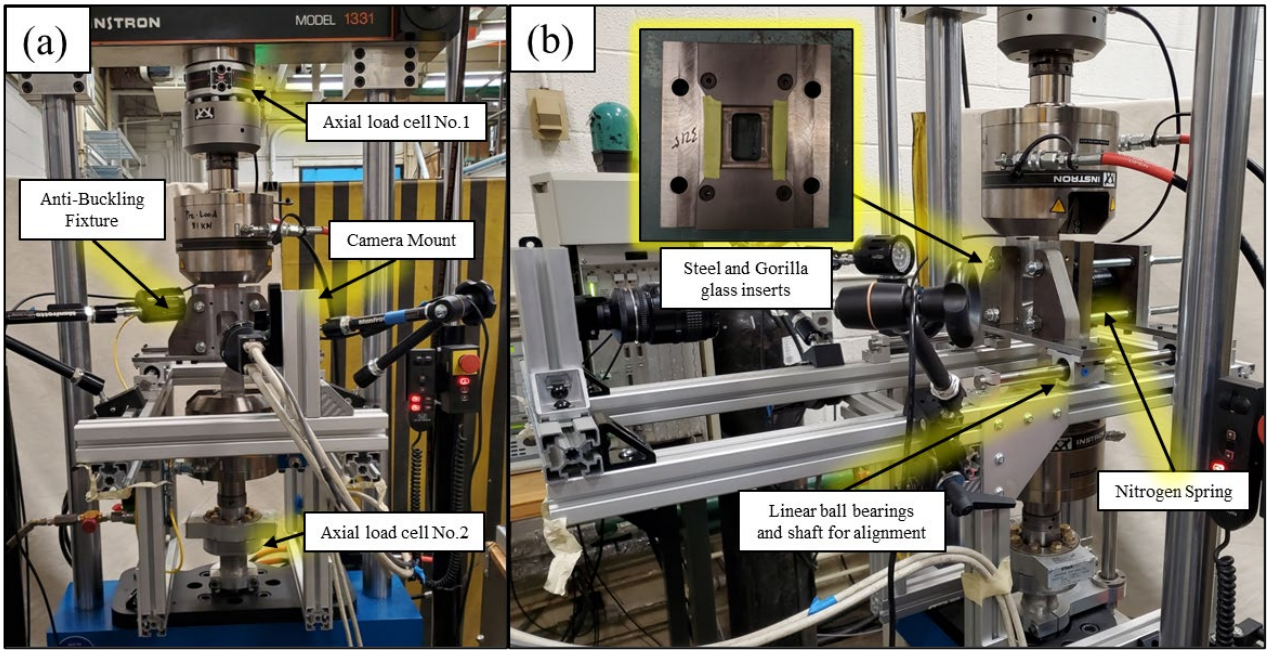


**Fig. 5.** (a) Front view and (b) side view of tension-compression test fixture.

To characterize chord modulus degradation, load-unload tests were performed using the sub-sized ASTM E8 [17] specimen geometry depicted in Fig. 1e. An AGX-V 50 kN Shimadzu® tensile frame with two Gazelle point Grey® cameras and 180 mm Tamron® lenses (Fig. 6) was used for stereo DIC, providing a resolution of 0.016 mm/pixel and 10 FPS sampling rate. Loading was performed using displacement control at intervals corresponding to approximately 1% strain. Fig. 7a depicts the unloading chord modulus degradation determined from load-unload testing. A linear fit of the data was performed over the range of 0.1% to 95% of the stress level at which the unloading occurred to obtain the chord modulus for a given load-unloading step. Furthermore, Fig. 7b depicts the measured Poisson's ratio which appears to remain constant with plastic strain. Although more sophisticated test methods, including electrical-resistance, ultrasonic strain-gauges, and impulse excitation are widely suggested in literature for measuring elastic properties [29-32], the measured saturation modulus ($E_s$) of 64.46 GPa is comparable with the reported values of 63 and 66.6 GPa for 6xxx-T4 aluminum in the work of Meng *et al*. [33] and Banerjee *et al.* [34].

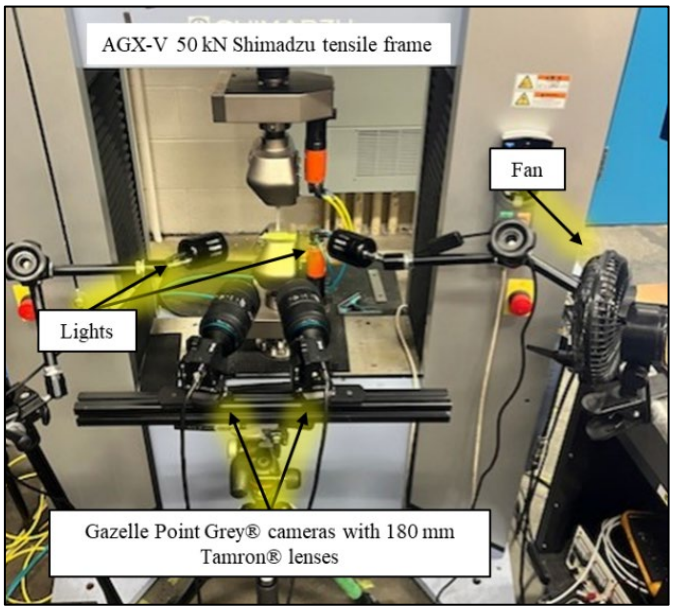


**Fig. 6.** Load-unload test setup used to characterize chord modulus degradation.

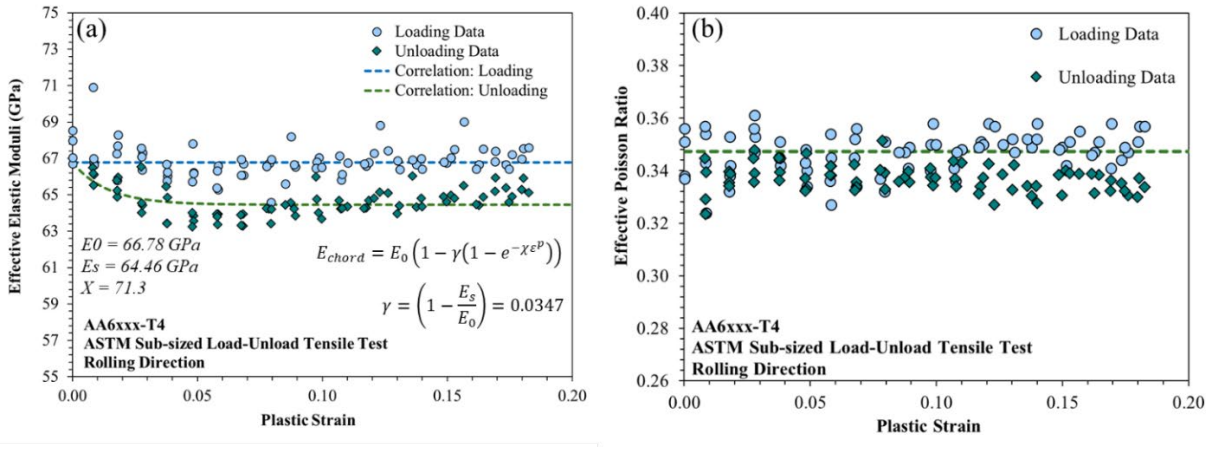


**Fig. 7.** (a) Unloading chord modulus degradation and (b) effective Poisson ratio for the AA6xxx-T4 alloy.

A single compression-tension cycle was input into AutoForm R12 to calibrate the transient softening rate ($\varkappa$) and stagnation ratio ($\xi$) parameters of the four-parameter AutoForm kinematic hardening model. Young's reduction factor ($\gamma$) and Young's reduction rate ($\chi$) were determined through the load-unload test. The AutoForm calibrated kinematic hardening curve is shown in Fig 8. and Table 3 summarizes the four AutoForm kinematic hardening parameters of the AA6xxx-T4 material.

**Table 3.** AutoForm kinematic hardening parameter values for the AA6xxx-T4 alloy using a CT cycle at 5.5% reversal strain.

| Parameter | Value |
|---|---|
| Transient Softening Rate ($\varkappa$) | 0.002 |
| Stagnation Ratio ($\xi$) | 0.280 |
| Young's Reduction Factor ($\gamma$) | 0.0347 |
| Young's Reduction Rate ($\chi$) | 71.3 |

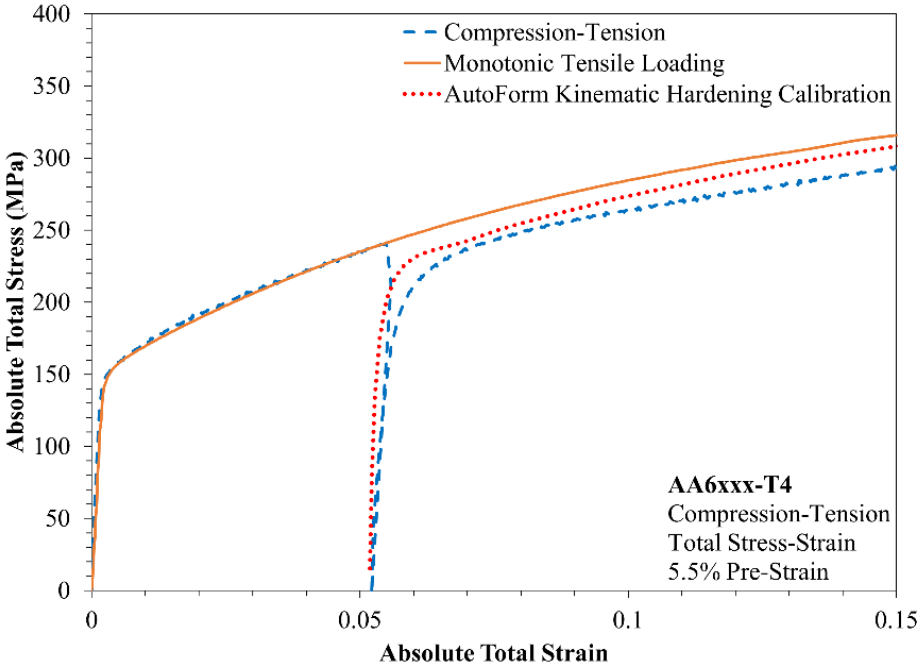


**Fig. 8.** Representative compression-tension cycle overlayed with monotonic tensile loading and AutoForm calibrated kinematic hardening curve.

Formability was characterized by performing Marciniak and Nakazima tests according to ISO 12004-2 [35] standard to generate a hybrid Marciniak-Nakazima forming limit curve (FLC) with the forming limits illustrated in Fig. 9a. The limit strains were determined for each specimen using five DIC line slices placed perpendicular to the crack location. The Marciniak tests were performed for five different strain paths, ranging from uniaxial tension to plane strain tension, using the same tooling described in Noder and Butcher [36]. In the Marciniak tests, stainless steel shim rings of 2.66 mm thickness were placed along the outer edge of the test specimens (Fig. 9b) to avoid lockbead splitting, resulting in a lockbead penetration depth of 1.94 mm. Nakazima tests were also performed for three different strain paths ranging between plane strain tension to biaxial stretching. Although Marciniak tests are preferred for minimizing process effects present in Nakazima tests related to non-linear strain paths, through thickness shear, and contact pressure [36]. A hybrid FLC was employed due to challenges of larger width test specimens experiencing cracking at the Marciniak punch radius. The specimen widths used in Marciniak and Nakazima tests are summarized in Table 4. The process effects present in Nakazima test may contribute to larger forming limit strains on the stretch side of the FLC (Fig. 9a).

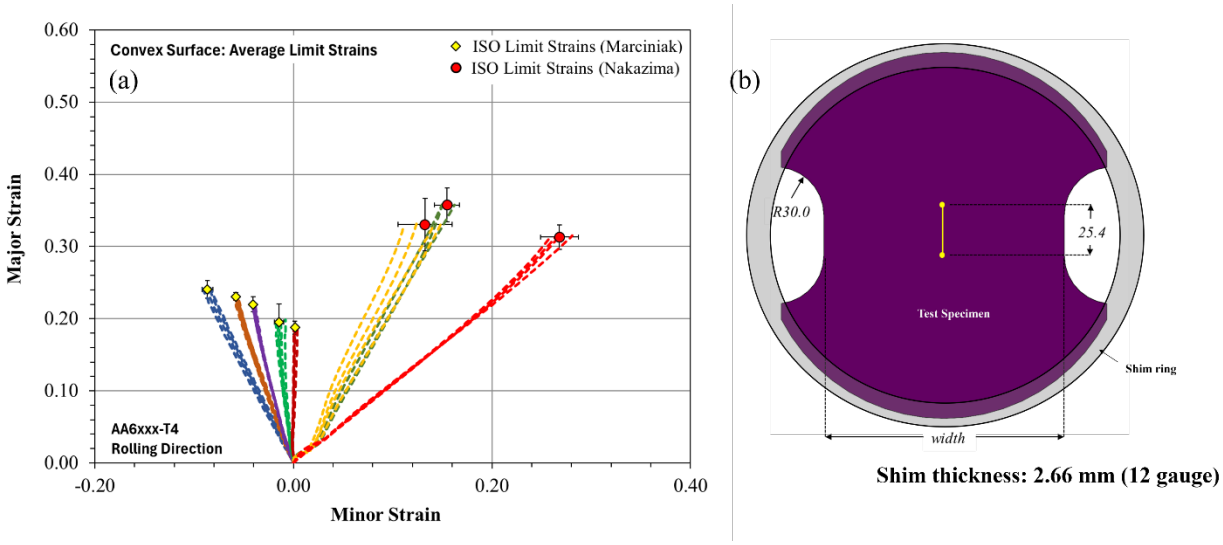


**Fig. 9.** (a) Hybrid Marciniak-Nakazima forming limit strains determined using ISO 12004-2 methodology. (b) Representative test specimen with circular shim ring used for Marciniak testing, all units in mm.

**Table 4.** FLC specimen widths used for Marciniak and Nakazima tests.

| | Specimen Width [mm] | | | | |
|---|---|---|---|---|---|
| **Marciniak Test** | 40 | 80 | 100 | 120 | 130 |
| **Nakazima Test** | 150 | 160 | 203 | | |

## 3. U-Shaped Rail Forming

The technology demonstrator U-shaped rail component developed by Novelis, shown in Fig. 10a, was formed using the blank geometry shown in Fig. 10b. The tooling used for the forming of these components features 2 mm drawbeads and 11.5 mm stakebeads and is shown in Fig. 11. The AA6xxx-T4 blanks were first laser cut and cleaned of any residual mill oil using acetone. Surface roughness measurements were then taken in the RD and TD directions using a Taylor Hobson Surtronic 25 linear profilometer and are summarized in Table 5. Hot-melt lubricant DC2-90 from Quaker Houghton was then applied uniformly onto the blank to an oversaturated state (>3 g/m$^2$) and verified using an Infralytic® NG2 oil sensor with an average measurement of 4.1 g/m$^2$ from several locations on the blank. The saturation state is defined as the maximum amount of lubricant the material can hold. Lubricant was applied beyond the saturation state to ensure the entirety of the blank was thoroughly lubricated.

**Table 5.** Average surface roughness measurements of AA6xxx-T4 blanks used for U-shape rail forming.

| | Rolling Direction (RD) | Transverse Direction (TD) |
|---|---|---|
| **$R_a$ [µm]** | 0.12 | 0.2 |
| **$R_z$ [µm]** | 0.8 | 1.1 |

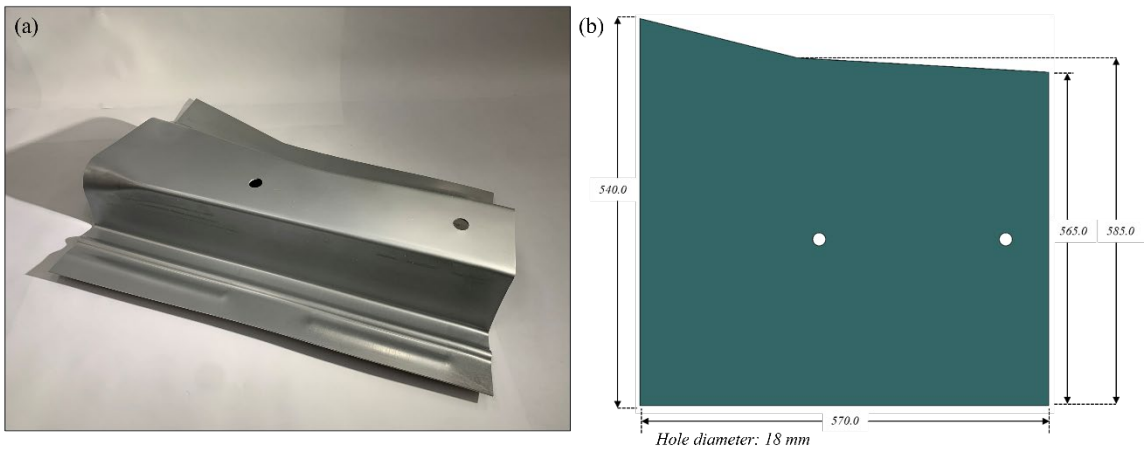


**Fig. 10.** (a) Isometric view of U-shaped rail formed using 2 mm AA6xxx-T4 and (b) blank geometry used to form U-shaped rail. All dimensions in mm.

Surface roughness measurements of the tooling were taken using a linear profilometer in four regions, shown in Fig. 11a, the average $R_a$ and $R_z$ roughness values from the measured tooling locations are 0.68 ± 0.22 µm and 3.88 ± 1.21 µm respectively. The binder tooling was fitted with four Dadco UX-20000.160 nitrogen springs with an initial pressure of 8963.18 kPa (1300 psi). This resulted in a variable binder force of 475.9 – 731.1 kN throughout the cushion stroke.

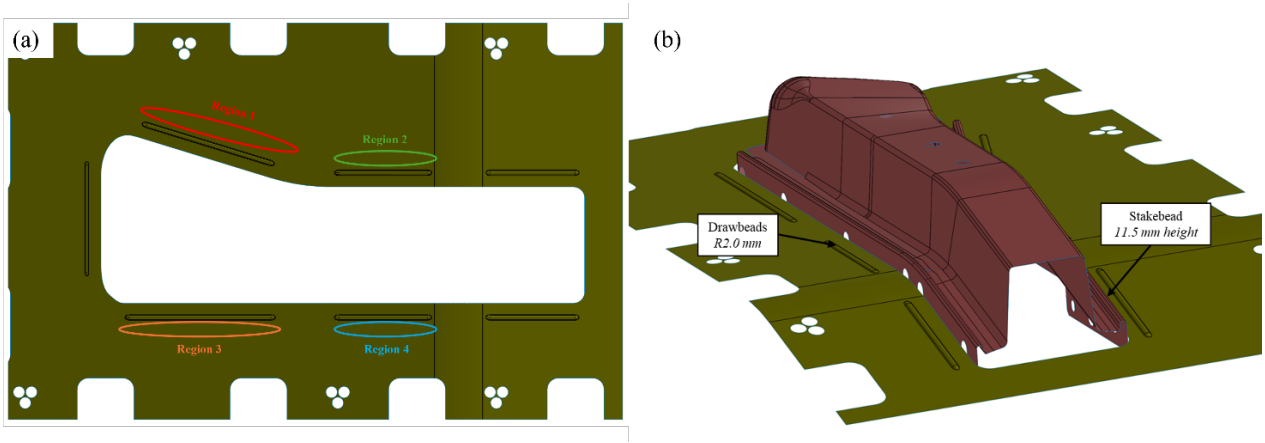


**Fig. 11.** (a) Schematic of binder surface indicating surface roughness measurement regions and (b) isometric view of binder and punch surfaces.

The U-shaped rails were formed successfully without any splits, necking, or excessive thinning observed in any region of the components. Following the stamping operation, ultrasonic thickness measurements were taken at twenty-one specified locations along the upper radius and side walls. The locations of these points were labeled in alphabetical order from A-U, with points I-K and S-U located on the side walls, and all other points located on the upper radius as shown in Fig. 12a. Approximately twenty-four hours after forming, components were then scanned using a 3D-white light scanner to assess final component shape after springback. The scanned surface was then imported back into AutoForm and positioned using the upper die surface. To quantify springback, multiple measurement strategies were utilized: (i) separation distance, which is defined as the normal distance from the resulting simulation surface to the scanned geometry; (ii) measured sprung punch and die radii, and (iii) flange angle after springback. The following measurement procedures are adapted from the 2022 Numisheet benchmark that used a similar U-shaped channel geometry [37]. Four cross sections were taken of the U-shaped rail at locations shown in Fig. 12b and following Zhou and Kannan [38], the sprung punch radii, die radii, and flange angles were measured at the four cross-sections.

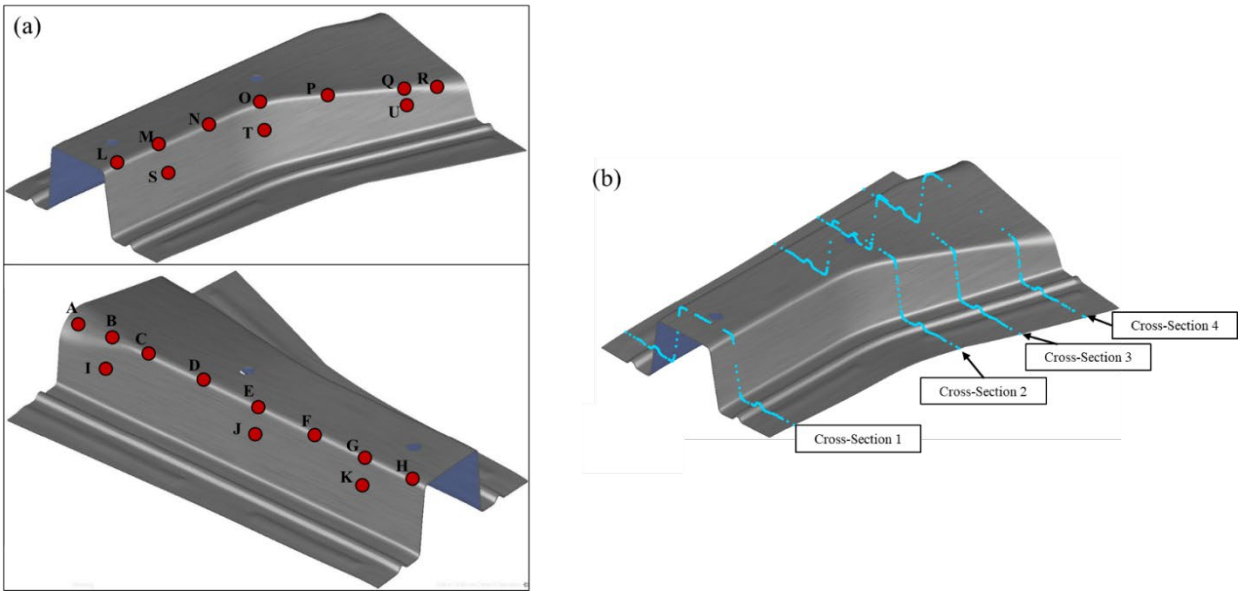


**Fig. 12.** (a) Twenty-one ultrasonic thickness measurement locations A-U and (b) four cross-section locations.

## 4. Finite Element Simulations

To assess the influence of different FE model parameters on thickness and springback predictions, the following simulation parameters were varied: maximum element angle (MEA), the initial element size (IES), initial subdivision level, and the addition of refinement zones (RZ). Two simulation trials featured refinement zones in the regions of the blank that contact the drawbeads, as shown in Fig. 13. A summary of model parameters investigated are outlined in Table 6. All simulations were conducted using the EPS-11 element type and BBC2005 material model.

**Table 6.** Summary of FE model parameters investigated in simulation of U-shaped rail forming operation. All other variables not specified were set to standard final validation (FV) values. *Specified within refinement zone. **Elements at end of simulation.

| Simulation parameters | Master elem. size [mm] | Max elem. angle [°] | Initial subdivision level | Max refinement level | No. of Elements** [x1000] |
|---|---|---|---|---|---|
| Final validation (FV) | 40.0 | 22.5 | Half | 6 | 78.7 |
| FV+MEA 20 deg | 40.0 | 20.0 | Half | 6 | 92.1 |
| FV+MEA 10 deg | 40.0 | 10.0 | Half | 6 | 388.2 |
| FV+MEA 5 deg | 40.0 | 5.0 | Half | 6 | 1.45E3 |
| IES 2.5 mm | 2.5 | 22.5 | Equal to master | 0 | 104.3 |
| IES 1.25 mm | 1.25 | 22.5 | Equal to master | 0 | 413.3 |
| FV+RZ MEA 10 deg | 40.0 | 10.0* | Half | 6 | 131.2 |
| FV+RZ MEA 5 deg | 40.0 | 5.0* | Half | 6 | 310.2 |

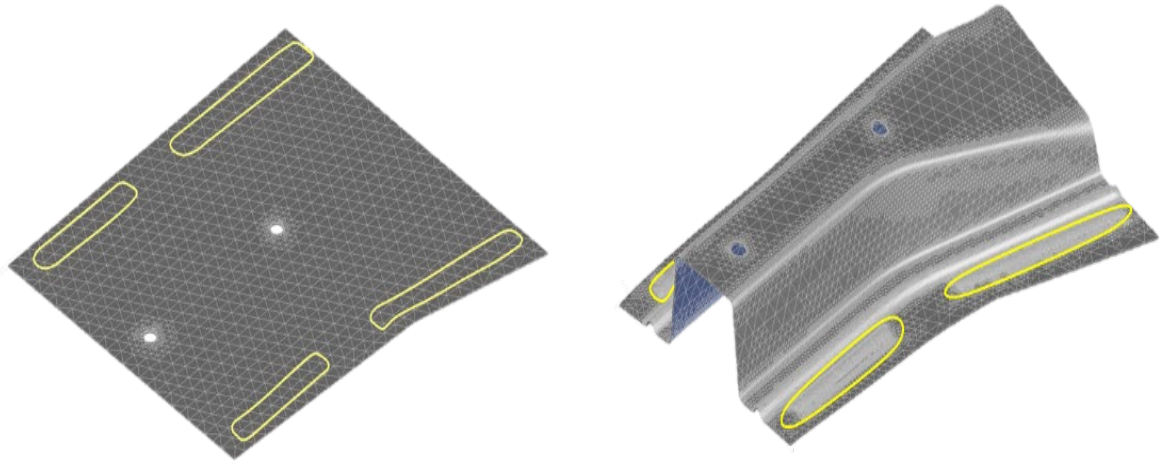

**Fig. 13.** Refinement zones (RZ) which flow over drawbeads. Elements outside these regions are refined using FV settings.

For assessing the effect of hardening model, friction model, and binder loading, eight model permutations within AutoForm were investigated and outlined in Table 7. The binder nitrogen spring locations were modeled using the "column binder loading" condition. Fig. 14a illustrates the tooling setup within the model, including the column locations on the binder surface. A constant coulomb coefficient of friction (μ) of 0.11 was selected in accordance with the established practice of the industrial project partners for the same material-lubricant system and is comparable with reported values of 0.12 for similar forming conditions in the work of Bolay *et al*. [15] and Berahmani *et al*. [16]. TriboForm AA6xxx mill finish-hot melt friction model provided in the TriboForm database, was fitted using the measured blank roughness, average tooling roughness, and the maximum lubrication amount of 3 g/m$^2$ to reflect the oversaturated lubricant condition. A 3D-surface plot of the fitted TriboForm friction model depicting friction coefficient versus pressure and sliding velocity is shown in Fig. 14b. The effect of kinematic hardening was investigated using the calibrated parameters previously outlined. For clarity, the following abbreviations are used: uniform binder loading (UL), column binder loading (CL), constant coulomb friction (CC), TriboForm (TF), isotropic hardening (IH), and kinematic hardening (KH).

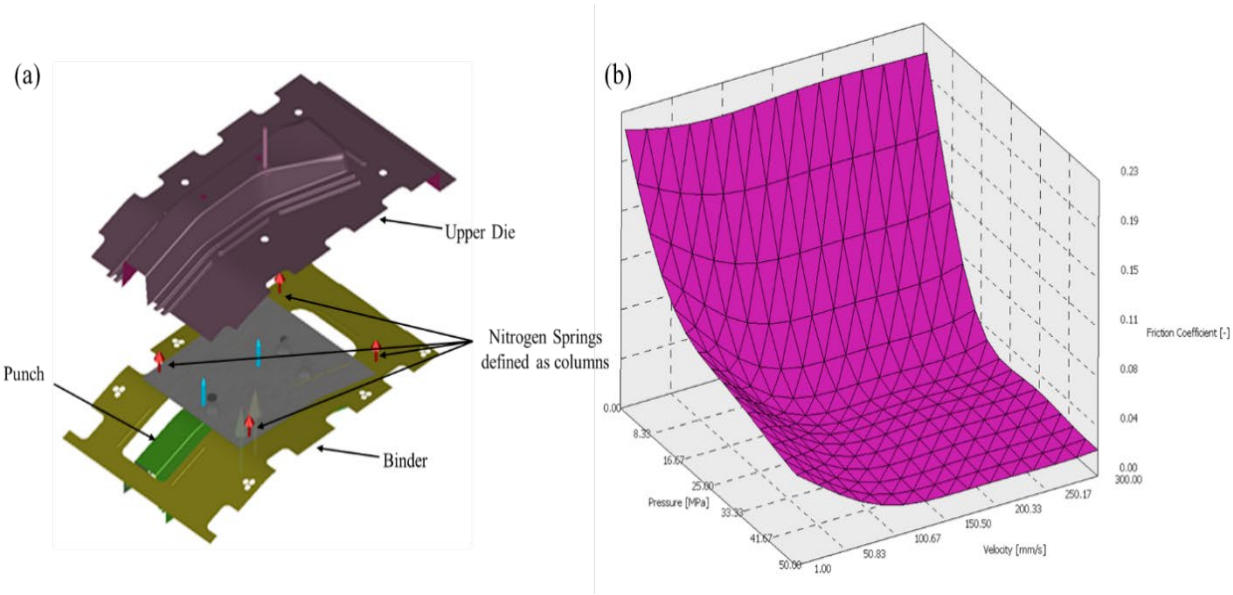


**Fig. 14.** (a) AutoForm FE-model setup of U-shaped rail forming operation, and (b) 3D plot of fitted TriboForm AA6xxx mill finished hot-melt friction model.

**Table 7.** Summary of model variants investigated in AutoForm R12.

| Model No. | Binder Loading | Friction Model | Hardening Model |
|---|---|---|---|
| Model 1 (UL-CC-IH) | Uniform | Constant Coulomb (μ = 0.11) | Isotropic |
| Model 2 (UL-TF-IH) | Uniform | TriboForm | |
| Model 3 (CL-CC-IH) | Column | Constant Coulomb (μ = 0.11) | |
| Model 4 (CL-TF-IH) | Column | TriboForm | |
| Model 5 (UL-CC-KH) | Uniform | Constant Coulomb (μ = 0.11) | Kinematic |
| Model 6 (UL-TF-KH) | Uniform | TriboForm | |
| Model 7 (CL-CC-KH) | Column | Constant Coulomb (μ = 0.11) | |
| Model 8 (CL-TF-KH) | Column | TriboForm | |

## 5. Results and Discussion

Using Model 1 (UL-CC-IH), the simulation parameters outlined in Table 6 were compared for thickness and springback correlation with the experimentally measured geometry. For the predicted thickness, the root mean squared error (RMSE) at locations A-U were compared. The proportion (%) of the sprung sheet surface that is within the bounds of material thickness (± 2 mm) to the scanned surface of the physical panel was defined as the separation distance and used as a general metric to quantify springback correlation. The thickness RMSE, separation distance and maximum material displacement after springback, which is a measure of the overall magnitude of springback, for the various simulation parameters are summarized in Table 8. The standard AutoForm final validation (FV) settings provided the best agreement for both thickness and springback predictions. An additional advantage of using the standard FV settings is the comparatively short computation time relative to the alternative settings evaluated in this study. As a result, the standard FV settings were adopted for all subsequent simulations.

**Table 8.** RMSE of thickness predictions and proportion of separation distance +/- 2 mm from scanned geometry for various control parameters investigated using Model 1.

| Simulation Parameters | Predicted Thickness RMSE [mm] | Separation Distance ±2 mm [%] | Max Material Displacement [mm] | Total CPU Time [min] |
|---|---|---|---|---|
| Final validation (FV) | 0.055 | 50.7 | 14.76 | 13.80 |
| FV+MEA 20 deg | 0.062 | 40.3 | 13.07 | 23.98 |
| FV+MEA 10 deg | 0.105 | 59.9 | 11.63 | 177.58 |
| FV+MEA 5 deg | 0.169 | 39.9 | 10.20 | 1330.11 |
| IES 2.5 mm | 0.053 | 44.3 | 15.80 | 85.82 |
| IES 1.25 mm | 0.077 | 54.5 | 12.72 | 1240.20 |
| FV+RZ MEA 10 deg | 0.062 | 42.6 | 12.72 | 27.20 |
| FV+RZ MEA 5 deg | 0.063 | 35.9 | 12.18 | 94.58 |

The eight model variants specified in Table 7 were investigated for formability, thickness, and springback predictive accuracy. The formability results of all eight model variants were properly captured, with no regions of predicted splitting, consistent with the forming trials. The models using Coulomb friction predicted a higher risk of splits, with some regions of the component within 20% of the FLC. This is highlighted in Fig. 15, which depicts the advanced formability contour plots of Model 1 (UL-CC-IH) and Model 8 (CL-TF-KH).

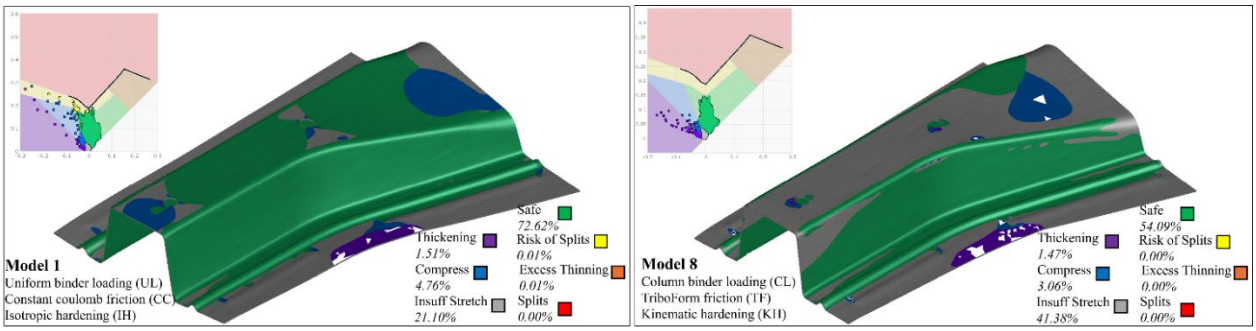


**Fig. 15.** Advanced formability contour plots of Model 1 and Model 8, shown on left and right respectively.

The predicted final thickness of the eight model variants was compared to the experimentally measured values at measurement locations A-U and are shown in Fig. 16a. Thickness predictions from Model 8 (CL-TF-KH) show improved agreement, with a RMSE of 0.044 mm versus 0.055 mm for Model 1 (UL-CC-IH). The proportion of separation distance within the bounds of material thickness is shown in Fig. 16b. When comparing the separation distance result of Model 1 (UL-CC-IH) to Model 3 (CL-CC-IH), it can be observed that the addition of column binder loading improved the springback correlation by 11.3 percentage points. This is further increased by 40.5 percentage points with the addition of the TriboForm friction model. Column binder loading paired with TriboForm friction models provided the best final thickness and springback predictions, as the frictional and tooling forces are better represented. These forces govern the flow of material into the die cavity, controlling the through thickness stress and strain gradients which are determining factors of thinning and final shape after springback. This is highlighted by Models 4 (CL-TF-IH) and 8 (CL-TF-KH) in Fig. 16. Note that the results of Models 2 (UL-TF-IH) and 6 (UL-TF-KH) were not included for conciseness, as their results were similar to Models 1 and 5 respectively.

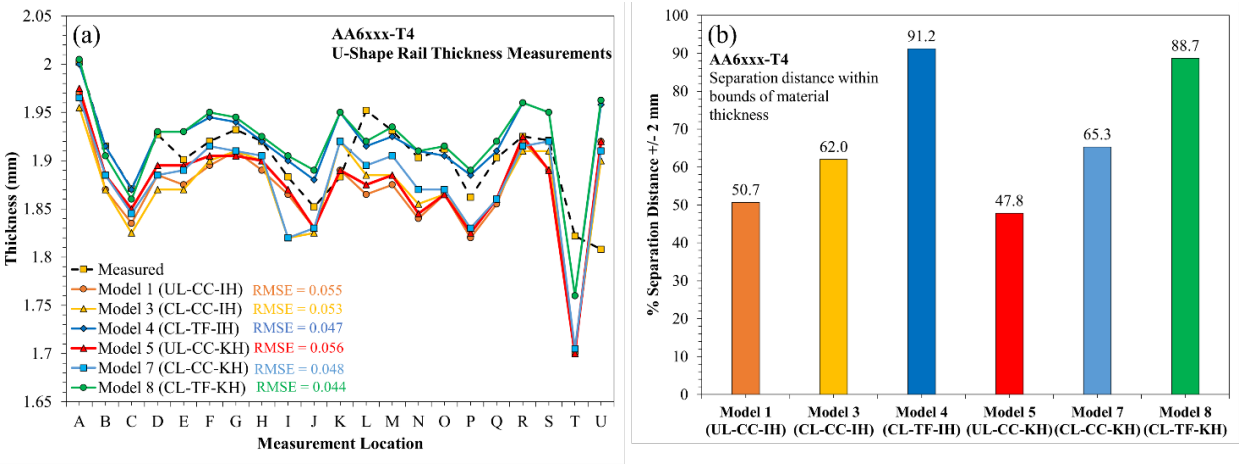


**Fig. 16.** (a) Ultrasonic thickness measurements and predicted final thicknesses at locations A-U and (b) percentage of separation distance +/- 2 mm from scanned geometry for various models.

Table 9 presents the percent error of the sprung die and punch radii between the scanned geometry for Models 1, 4, and 8. Fig. 17a illustrates the measured and predicted flange angle for Models 1, 4 and 8, with a representative cross-section plot used for the various measurements as shown in Fig. 17b. Models 4 (CL-TF-IH) and 8 (CL-TF-KH) are emphasized due to their better correlation with the separation distance. Model 1 (UL-CC-IH) is used as a reference as it is the simplest of all model variants analyzed. Kinematic hardening (Model 8) marginally improves springback predictive accuracy of sprung punch and die radii compared to isotropic hardening (Model 4). Kinematic hardening also appears to increase the overprediction of flange angle after springback. It should be noted that alternative kinematic hardening models and calibration over additional pre-strain ranges may have a greater influence on springback predictions. Additionally, time-dependent effects, as shown by Wang *et al.* [39], may contribute to discrepancies as components were scanned twenty-four

hours after forming and such effects are not considered in models. Furthermore, when comparing the results of Model 4 (CL-TF-IH) and 8 (CL-TF-KH) to that of Model 1 (UL-CC-IH) the predicted flange angle after springback shows a significant improvement.

**Table 9.** Percent error of sprung die and punch radii for Models 1, 4, and 8 at four cross-section locations.

| | Model 1 (UL-CC-IH) | | Model 4 (CL-TF-IH) | | Model 8 (CL-TF-KH) | |
|---|---|---|---|---|---|---|
| **Cross Section No.** | **Die Radii Error [%]** | **Punch Radii Error [%]** | **Die Radii Error [%]** | **Punch Radii Error [%]** | **Die Radii Error [%]** | **Punch Radii Error [%]** |
| Section 1 | 10.3 | 4.4 | 3.4 | 3.2 | 2.4 | 0.4 |
| Section 2 | 6.2 | 6.3 | 9.2 | 1.7 | 11.3 | 0.6 |
| Section 3 | 15.5 | 24.6 | 15.5 | 16.2 | 15.4 | 19.6 |
| Section 4 | 1.1 | 5.1 | 7.4 | 4.5 | 2.4 | 3.9 |
| **Average** | **8.3** | **10.1** | **8.9** | **6.4** | **7.9** | **6.1** |

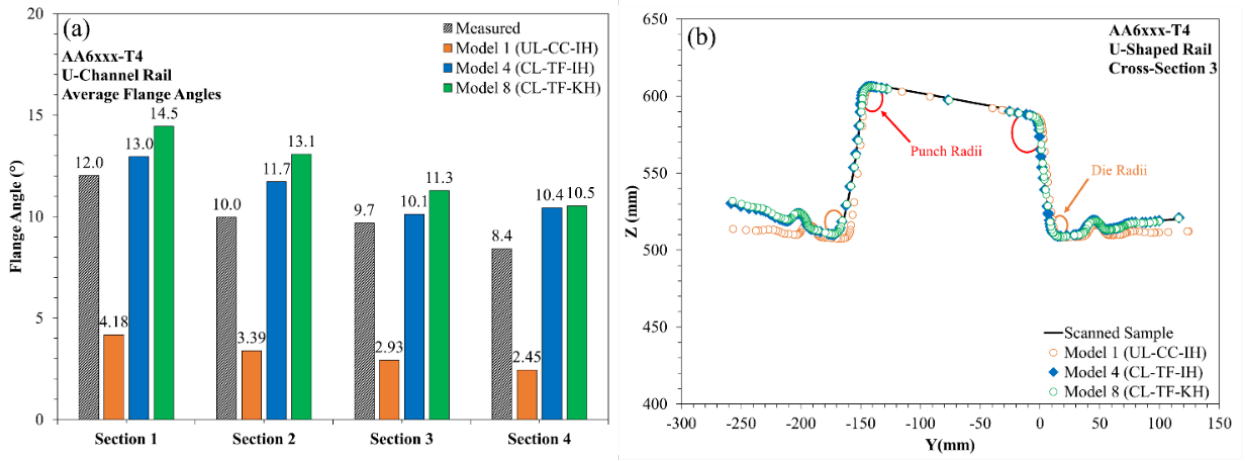


**Fig. 17.** (a) Average of left and right flange angles of scanned and predicted geometries of Models 1, 4, and 8, (b) Cross-section 3 depicting the scanned geometry overlayed with Models 1, 4, and 8.

## 6. Summary and Conclusion

The primary conclusions that can be drawn from this experimental-numerical study are:

- The standard AutoForm final validation (FV) control parameters provided the best balance of both simulation time and predictive accuracy of thinning, formability, and final shape after springback.
- Accurately representing the tooling force distribution through specified binder spring locations is paramount in predicting material thinning and final shape after springback. The addition of column binder loading alone increased springback prediction accuracy by 11.3 and 17.5 percentage points in the case of isotropic and kinematic hardening respectively.
- Independently, kinematic hardening marginally improved springback and final thickness predictions for the AA6xxx-T4. However, the use of alternative kinematic hardening models and the calibration over additional strain ranges may reveal a stronger effect on springback.
- The marginal improvement kinematic hardening provided is secondary to accurately capturing friction, which controls the flow of material into the die cavity.
- Future work should consider potential time-dependent springback effects with geometry measurements taken immediately after forming as well as 24 hours after.
- TriboForm friction model with column binder loading provided the most significant improvement for springback predictions. This combination reduced RMSE of thickness predictions by 0.011 mm and improved the separation distance metric by 40.5 percentage points.

**Acknowledgement**

Funding of this work was provided by the Natural Sciences and Engineering Research Council of Canada (NSERC). The authors would like to acknowledge the technical support provided by AutoForm Engineering USA. Special appreciation is extended to Prof. Jacqueline Noder of the University of British Columbia for her continued technical guidance throughout this work. The authors would like to further express their gratitude to Garrett Klein and Ryan Bowerman of Novelis Novi for their technical assistance during forming trials and for conducting the white-light scanning of formed components.

**References**

[1] W. Zhang and J. Xu, "Advanced lightweight materials for automobiles: A Review," *Materials & Design*, vol. 221, p. 110994, Sep. 2022. doi:10.1016/j.matdes.2022.110994.

[2] I. N. Fridlyander *et al.*, "Aluminum alloys: Promising materials in the automotive industry," *Metal Science and Heat Treatment*, vol. 44, no. 9–10, pp. 365–370, Sep. 2002. doi:10.1023/a:1021901715578.

[3] X. Guo, Y. Gu, H. Wang, K. Jin, and J. Tao, "The bauschinger effect and mechanical properties of AA5754 aluminum alloy in incremental forming process," *The International Journal of Advanced Manufacturing Technology*, vol. 94, no. 1–4, pp. 1387–1396, Aug. 2017. doi:10.1007/s00170-017-0965-y.

[4] H. Ul Hassan, H. Traphöner, A. Güner, and A. E. Tekkaya, "Accurate springback prediction in deep drawing using pre-strain based multiple cyclic stress–strain curves in finite element simulation," *International Journal of Mechanical Sciences*, vol. 110, pp. 229–241, May 2016. doi:10.1016/j.ijmecsci.2016.03.014.

[5] P.-A. Eggertsen and K. Mattiasson, "On the identification of kinematic hardening material parameters for accurate springback predictions," *International Journal of Material Forming*, vol. 4, no. 2, pp. 103–120, Dec. 2010. doi:10.1007/s12289-010-1014-7.

[6] P. Solfronk, J. Sobotka, and D. Korecek, "Utilization of advanced computational methods to predict spring-back of aluminium alloys in automotive industry," *Manufacturing Technology*, vol. 20, no. 1, pp. 98–103, Aug. 2020. doi:10.21062/mft.2020.006.

[7] F. Yoshida and T. Uemori, "A model of large-strain cyclic plasticity describing the bauschinger effect and workhardening stagnation," International Journal of Plasticity, vol. 18, no. 5–6, pp. 661–686, Oct. 2002. doi:10.1016/s0749-6419(01)00050-x.

[8] H. J. Bong, J. Lee, and M.-G. Lee, "Finite element modeling of springback behaviour for aluminum 6000 series sheets using three-point bending tests," *International Journal of Automotive Technology*, vol. 26, no. 5, pp. 1285–1294, May 2025. doi:10.1007/s12239-025-00260-6.

[9] J.-Y. Lee, F. Barlat, and M.-G. Lee, "Constitutive and friction modeling for accurate springback analysis of Advanced High Strength Steel Sheets," *International Journal of Plasticity*, vol. 71, pp. 113–135, Aug. 2015. doi:10.1016/j.ijplas.2015.04.005.

[10] J. Y. Lee, "Evaluation of Constitutive Models for Springback Prediction in U-draw/bending of DP and TRIP Steel Sheets," thesis, Pohang University of Science and Technology, Pohang, 2011.

[11] I. Gil, J. Mendiguren, L. Galdos, E. Mugarra, and E. Saenz de Argandoña, "Influence of the pressure dependent coefficient of friction on deep drawing springback predictions," *Tribology International*, vol. 103, pp. 266–273, Nov. 2016. doi:10.1016/j.triboint.2016.07.004.

[12] W. MA, B. WANG, L. FU, J. ZHOU, and M. HUANG, “Effect of friction coefficient in deep drawing of AA6111 sheet at elevated temperatures,” *Transactions of Nonferrous Metals Society of China*, vol. 25, no. 7, pp. 2342–2351, Jul. 2015. doi:10.1016/s1003-6326(15)63849-3.

[13] M. Mohamed, M. Farouk, A. Elsayed, M. Shazly, and A. A. Hegazy, “An investigation of friction effect on formability of AA 6061-T4 sheet during cold forming condition,” *AIP Conference Proceedings*, vol. 1892, p. 080025, 2017. doi:10.1063/1.5008105.

[14] Y. Gao, H. Li, D. Zhao, M. Wang, and X. Fan, “Advances in friction of aluminium alloy deep drawing,” *Friction*, vol. 12, no. 3, pp. 396–427, Jul. 2023. doi:10.1007/s40544-023-0761-7.

[15] C. Bolay *et al.*, “Friction modelling in sheet metal forming simulations for aluminium body parts at Daimler AG,” *IOP Conference Series: Materials Science and Engineering*, vol. 651, no. 1, p. 012104, Nov. 2019. doi:10.1088/1757-899x/651/1/012104.

[16] S. Berahmani, C. Bilgili, G. Erol, J. Hol, and B. Carleer, “The effect of friction and lubrication modelling in stamping simulations of the ford transit hood inner panel: A numerical and experimental study,” *IOP Conference Series: Materials Science and Engineering*, vol. 967, no. 1, p. 012010, Nov. 2020. doi:10.1088/1757-899x/967/1/012010.

[17] ASTM International, "ASTM E8/E8M-25, Standard Test Methods for Tension Testing of Metals", 2025.

[18] A. Abedini, A. Narayanan, and C. Butcher, “A deterministic methodology to calibrate pressure-independent anisotropic yield criteria in plane strain tension using finite-element analysis,” Applied Mechanics, vol. 3, no. 3, pp. 905–934, Jul. 2022. doi:10.3390/applmech3030052.

[19] International Organization for Standardization, "ISO 16808:2022, Metallic materials - Sheet and strip - Determination of biaxial stressstrain curve by means of bulge test with optical measuring systems, 2022.

[20] A. Narayanan, A. Abedini, A. Weinschenk, M. J. Worswick, and C. Butcher, “Evaluation of simple shear test geometries for constitutive characterization using virtual experiments,” IOP Conference Series: Materials Science and Engineering, vol. 1157, no. 1, p. 012066, Jun. 2021. doi:10.1088/1757-899x/1157/1/012066.

[21] A. Narayanan et al., “Identification of the plane strain yield strength of anisotropic sheet metals using inverse analysis of Notch tests,” SAE Technical Paper Series, vol. 1, Mar. 2022. doi:10.4271/2022-01-0241.

[22] F. Barlat et al., “Plane stress yield function for aluminum alloy sheets-part 1: Theory,” International Journal of Plasticity, vol. 19, no. 9, pp. 1297–1319, Sep. 2003. doi:10.1016/s0749-6419(02)00019-0.

[23] D. Banabic, H. Aretz, D. S. Comsa, and L. Paraianu, “An improved analytical description of orthotropy in metallic sheets,” International Journal of Plasticity, vol. 21, no. 3, pp. 493–512, Mar. 2005. doi:10.1016/j.ijplas.2004.04.003.

[24] T. Kuwabara, T. Mori, M. Asano, T. Hakoyama, and F. Barlat, “Material modeling of 6016-O and 6016-T4 aluminum alloy sheets and application to hole expansion forming simulation,” *International Journal of Plasticity*, vol. 93, pp. 164–186, Jun. 2017. doi:10.1016/j.ijplas.2016.10.002.

[25] A. Abedini, A. Narayanan, and C. Butcher, “An investigation into the characterization of the hardening response of sheet metals using tensile and shear tests with surface strain measurement,” *Forces in Mechanics*, vol. 7, p. 100090, May 2022. doi:10.1016/j.finmec.2022.100090.

[26] J. M. Choung and S. R. Cho, “Study on true stress correction from tensile tests,” *Journal of Mechanical Science and Technology*, vol. 22, no. 6, pp. 1039–1051, Jun. 2008. doi:10.1007/s12206-008-0302-3.

[27] D. K. Banerjee, C. A. Calhoun, M. A. Iadicola, W. E. Luecke, and T. J. Foecke, “Toward development of optimum specimen designs and modeling of in-plane uniaxial compression testing of aluminum alloy 2024 and AISI 1008 steel sheet material,” *Journal of Physics: Conference Series*, vol. 1063, p. 012068, Jul. 2018. doi:10.1088/1742-6596/1063/1/012068.

[28] L. Pilozo-Hibbit, “Characterization of 6xxx Aluminum Alloys for Forming and Springback Simulations,” thesis, University of Waterloo, Waterloo, 2026.

[29] D. H. Chung and W. R. Buessem, “The voigt-reuss-hill approximation and elastic moduli of polycrystalline mgo, caf2, β-zns, ZnSe, and CdTe,” Journal of Applied Physics, vol. 38, no. 6, pp. 2535–2540, May 1967. doi:10.1063/1.1709944.

[30] H. M. Ledbetter and M. W. Austin, “Effects of carbon and nitrogen on the elastic constants of AISI Type 304 stainless steel,” Materials Science and Engineering, vol. 70, pp. 143–149, Apr. 1985. doi:10.1016/0025-5416(85)90275-7.

[31] V. Luzin, S. Banovic, T. Gnäupel-Herold, H. Prask, and R. E. Ricker, “Measurement and calculation of elastic properties in low carbon steel sheet,” Materials Science Forum, vol. 495–497, pp. 1591–1596, Sep. 2005. doi:10.4028/www.scientific.net/msf.495-497.1591.

[32] N. Deng and Y. P. Korkolis, “Elastic anisotropy of dual-phase steels with varying martensite content,” International Journal of Solids and Structures, vol. 141–142, pp. 264–278, Jun. 2018. doi:10.1016/j.ijsolstr.2018.02.028.

[33] Q. Meng, J. Zhao, Z. Mu, R. Zhai, and G. Yu, “Springback prediction of multiple reciprocating bending based on different hardening models,” Journal of Manufacturing Processes, vol. 76, pp. 251–263, Apr. 2022. doi:10.1016/j.jmapro.2022.01.070.

[34] D. K. Banerjee, W. E. Luecke, M. A. Iadicola, and E. Rust, “Evaluation of methods for determining the Yoshida-uemori combined isotropic/kinematic hardening model parameters from tension-compression tests of advanced lightweighting materials,” Materials Today Communications, vol. 33, p. 104270, Dec. 2022. doi:10.1016/j.mtcomm.2022.104270.

[35] International Organization for Standardization, "ISO 12004-2:2021, Metallic materials - Determination of forming-limit curves for sheet and strip - Part 2: Determination of forming-limit curves in the laboratory, 2021.

[36] J. Noder and C. Butcher, “A comparative investigation into the influence of the constitutive model on the prediction of in-plane formability for Nakazima and Marciniak Tests,” *International Journal of Mechanical Sciences*, vol. 163, p. 105138, Nov. 2019. doi:10.1016/j.ijmecsci.2019.105138.

[37] M. C. Oliveira, C. Gomes, D. M. Neto, J. L. Alves, and L. F. Menezes, “Influence of process and material parameters on the twist springback prediction of a panel,” *IOP Conference Series: Materials Science and Engineering*, vol. 1284, no. 1, p. 012067, Jun. 2023. doi:10.1088/1757-899x/1284/1/012067.

[38] D. J. Zhou and K. Kannan, The Effect of Combination Beads on Springback: Experimental Study & Virtual Study, presented at the GDIS Conference, 2021.

[39] J. F. Wang, R. H. Wagoner, W. D. Carden, D. K. Matlock, and F. Barlat, “Creep and Anelasticity in the springback of aluminum,” International Journal of Plasticity, vol. 20, no. 12, pp. 2209–2232, Dec. 2004. doi: 10.1016/j.ijplas.2004.05.008.